

Anomalous hydrogen dynamics of the ice VII–VIII transition revealed by high-pressure neutron diffraction

Kazuki Komatsu^{a,1}, Stefan Klotz^b, Shinichi Machida^c, Asami Sano-Furukawa^d, Takanori Hattori^d, and Hiroyuki Kagi^a

^aGeochemical Research Center, Graduate School of Science, The University of Tokyo, Bunkyo-ku, Tokyo 113-0033, Japan; ^bInstitut de Minéralogie, de Physique des Matériaux et de Cosmochimie, CNRS UMR 7590, Sorbonne Université, F-75252 Paris, France; ^cNeutron Science and Technology Center, CROSS, Tokai, Naka, Ibaraki 319-1106, Japan; and ^dJ-PARC Center, Japan Atomic Energy Agency, Tokai, Naka, Ibaraki 319-1195, Japan

Edited by Pablo G. Debenedetti, Princeton University, Princeton, NJ, and approved February 18, 2020 (received for review November 20, 2019)

Above 2 GPa the phase diagram of water simplifies considerably and exhibits only two solid phases up to 60 GPa, ice VII and ice VIII. The two phases are related to each other by hydrogen ordering, with the oxygen sublattice being essentially the same. Here we present neutron diffraction data to 15 GPa which reveal that the rate of hydrogen ordering at the ice VII–VIII transition decreases strongly with pressure to reach timescales of minutes at 10 GPa. Surprisingly, the ordering process becomes more rapid again upon further compression. We show that such an unusual change in transition rate can be explained by a slowing down of the rotational dynamics of water molecules with a simultaneous increase of translational motion of hydrogen under pressure, as previously suspected. The observed cross-over in the hydrogen dynamics in ice is likely the origin of various hitherto unexplained anomalies of ice VII in the 10–15 GPa range reported by Raman spectroscopy, X-ray diffraction, and proton conductivity.

ice | high pressure | neutron diffraction | order–disorder phase transition

Ice VII is a cubic crystal with fully disordered hydrogen arrangements, i.e., a given oxygen atom is tetrahedrally surrounded by two hydrogen atoms randomly distributed over four hydrogen sites (1). When cooled to below ~ 270 K, hydrogen ordering occurs to give tetragonal ice VIII where the molecular dipoles point toward the *c* axis. At pressures above ~ 70 GPa, the hydrogen bonds of ice VII and VIII are centered, i.e., hydrogen moves to exactly midpoint between two oxygen atoms to form ice X. At high temperatures and moderate pressures, simulations (2–5) predict a “plastic” phase with dynamic rotational disorder of water molecules, and further above a superionic phase with high hydrogen diffusivity. The latter involves translation motion of hydrogen as well as rotation of water molecules, as suggested by calculations (6–12) and experiments (13–15). In other words, the structural variety in ice polymorphs in the 2–100 GPa range is caused by the static and/or dynamic state of the hydrogen; ice VIII and ice X can be distinguished by their static hydrogen distribution, whereas ice VII, the plastic phase, and the superionic phase are characterized by their dynamic features (12).

Here we use neutron diffraction to probe the hydrogen dynamics of ice VII across the VII–VIII (i.e., disorder–order) boundary applying a fast-cooling method. It is empirically known that H-ordering occurs at 2 GPa within a fraction of a second and it is therefore believed that ice VII is unquenchable. On the other hand, metastable ice VII can exist in the stable region of ice VIII in cases of low-temperature compression of ice VI (16), or incorporating ionic species into ice VII structure (17–19). Therefore, if the timescale for H-ordering slows down under pressure and becomes comparable to the time necessary to cool the sample to temperature where the kinetics is frozen in, partially disordered ice VIII should be observable.

To investigate this possibility, we prepared several samples of ice VII at 300 K between 2.8 and 15.1 GPa, fast-cooled them isobarically at a rate of 6 K/min across the VII–VIII phase

boundary, and collected diffraction patterns of the obtained material at 93 K (Fig. 1). Experimental details are described in *Methods*, and the details of temperature change in cooling are given in *SI Appendix, Fig. S1*. We find indeed highly H-disordered phase VIII at around 10 GPa, but not for pressures significantly below and above. Our results are remarkable since they allow a direct link with recent high-pressure electric conductivity measurements: The low-frequency limit (corresponding to direct current [dc]) of electric conductivity in ice is associated with a proton diffusion requiring the combination of both rotational and translational hydrogen motions (e.g., ref. 20). Measurements of the dc electric conductivity of ice VII obtained from impedance spectroscopy show an increase of the electrical conductivity at least up to 4.18 GPa (21), a maximum at around 10 GPa (22), and exponentially decreasing proton-diffusion coefficients between 10 and 63 GPa (23). Also, diffusion coefficients of hydrogens in ice VII are recently reexamined from 5.5 to 17 GPa using Raman spectroscopy, finding a maximum of the coefficients at around 10 GPa (24).

Results and Discussion

The characteristic feature of ice VIII in the diffraction pattern is the doublet of the 103 and 211 Bragg reflections at ~ 1.9 Å which

Significance

We report high-pressure neutron data which reveal a highly unusual behavior of the hydrogen dynamics in ice under high pressure: The transition rate from hydrogen-disordered ice VII to ordered ice VIII slows down dramatically up to 10 GPa but becomes more rapid again above. This finding is quantitatively explainable by a competition between the rotational and translational dynamics of water molecules. Our findings reply to a long-standing problem of unexplained anomalies of ice VII in the 10–15 GPa range reported by Raman spectroscopy, X-ray diffraction, and proton conductivity. Since ice VII and ice VIII are prototypical hydrogen-bonded materials with order–disorder transition, the pressure-induced cross-over in the hydrogen dynamics found in this study might be commonly observable in other materials.

Author contributions: K.K. and S.K. conceived and designed the experiments; K.K., S.K., S.M., A.S.-F., T.H., and H.K. conducted the neutron diffraction experiments; K.K. analyzed the data; and K.K. and S.K. wrote the paper with contributions from all authors.

The authors declare no competing interest.

This article is a PNAS Direct Submission.

Published under the PNAS license.

Data deposition: The neutron diffraction patterns and crystallographic data for structures reported in this study have been deposited at the Cambridge Crystallographic Data Centre (CCDC), under deposition numbers 1988381–1988417.

¹To whom correspondence may be addressed. Email: kom@eqchem.s.u-tokyo.ac.jp.

This article contains supporting information online at <https://www.pnas.org/lookup/suppl/doi:10.1073/pnas.1920447117/-DCSupplemental>.

First published March 11, 2020.

is absent for ice VII. Inspection of our neutron-diffraction patterns obtained from samples which are across the VII–VIII phase boundary at various initial pressures reveals a remarkable feature (see Fig. 2A): the intensity of the doublet peaks decreases with increasing pressure up to ~10 GPa where it reaches almost zero, and then reappears upon further compression. This phenomenon must be related to hydrogen ordering because the intensity of the doublet ($l = \text{odd}$) is only produced by the hydrogen (deuterium) sublattice and is not affected by oxygen which remains at its position across the transition. Partial H-disorder in the ice VIII structure can be easily introduced by populating the D2 sites (blue spheres in Fig. 1) situated at $[0, 1 - y(\text{D1}), 2 \times z(\text{O}) - z(\text{D1}) + 1/4]$ and constraining the occupancy (occ) of D1 and D2 to $\text{occ}(\text{D2}) = 1 - \text{occ}(\text{D1})$. Note that this H-disorder model was adopted for the whole pressure range since no evidence for a different kind of ordering like recently discussed in the case of ice VI/XV (26–29) was found in any diffraction pattern of this study.

As already expected from the observed profile patterns (Fig. 2B), the refined occupancies of the D2 site show a maximum at ~10 GPa, reaching 0.351(5) at 10.17(6) GPa in Run1 and 0.275(4) at 11.12(4) GPa in Run2. Despite a small difference between Run1 and Run2, the increase in occupancy up to 10 GPa followed by a decrease at higher pressure is perfectly reproducible. Other structural parameters behave in a similar way: The axial ratio c/a and the displacement of oxygen atom from the ideal positions in the cubic structure $\varepsilon (= 2c [1/8 - z(\text{O})])$ both show a minimum at around 10 GPa (Fig. 2C and D, also summarized in Table 1). In fact, the minimum value of c/a [1.4239(2)] and that of ε [0.082(2)] are close to $\sqrt{2}$ and 0, respectively, i.e., close to the values for oxygen on an ideal cubic sublattice. The behavior of these quantities is hence consistent with the occurrence of partial H-disorder as concluded from the Bragg intensities.

The refinement for the sample annealed at 11.48(7) GPa and 260 K for 2 h (no. 30659 in Run1), the one which was before rapid-cooled to 93 K at 11.34(6) GPa (no. 30657), shows a disappearance of H-disorder and a transformation to nearly completely ordered ice VIII, visible in the diffraction patterns (Fig. 3) by a reappearance of the intensities of the doublet at ~1.9 Å. It is uncertain whether the residual occupancy of the D2 site [0.041(4)] is statistically meaningful because the χ^2 for the Rietveld refinements

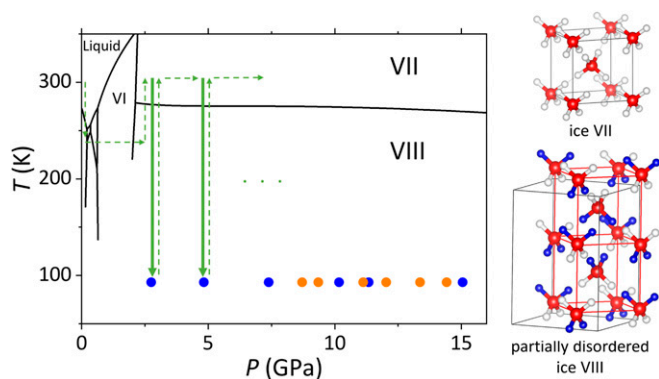


Fig. 1. (Left) Phase diagram of ice with the representative P - T path in the present experiments (green dashed and solid arrows) and (Right) crystal structures of ice VII and partially disordered ice VIII. Phase boundaries of ice polymorphs are based on previous studies compiled by Dunaeva et al. (25). Blue and orange circles in the left figure shows P - T points where neutron-diffraction patterns were obtained in Run1 and Run2, respectively (see also Table 1) after fast cooling from 300 K across the ice VII–VIII phase boundary (solid arrows). Red and white balls in the right figures are oxygen and hydrogen, respectively. Blue balls in ice VIII show additional sites (D2) partially occupied by hydrogens. Black lines depict the unit cells of ice VII and VIII and red lines in ice VIII the body-centered cubic oxygen sublattice corresponding to the unit cell of ice VII.

based on this partially disordered model ($\chi^2 = 1.329$) and a fully ordered model ($\chi^2 = 1.356$) show no significant difference. In any case, it is unquestionable that the occupancy of D2, the c/a ratio, and ε for the annealed sample are very different compared to the rapidly cooled sample (Fig. 2), which clearly shows that the partially disordered ice VIII is a transient state caused by rapid cooling. Therefore, the observed maximum/minimum in the refined structural parameters clearly has its origin in the slowing down of the kinetics of the ice VII to VIII transition under compression to 10 GPa.

The order–disorder phase transition in ice is controlled by the kinetics of hydrogen motion, which can be classified as two kinds of motion, i.e., 1) the rotation of water molecules and 2) the translational movement of hydrogen along H-bonds. While the dc electrical conductivity (22) and macroscopic proton diffusion—as detected in Raman data (24)—is mainly controlled by the slower of the two processes (20, 30, 31), the rate-determining process in the order–disorder transition (as probed in this study) should be the faster one. This is because an order–disorder transition does not require a cooperative motion of hydrogens, contrary to dc conductivity (22) and macroscopic proton-diffusion phenomena (24).

Here we propose a model which is able to reproduce the observed phenomena by assuming that rotational movements in ice VII slow down with increasing pressure whereas the translation process accelerates, resulting in a cross-over at around 10 GPa (22, 24, 32, 33). Based on the idea that both rotational and translational motions contribute to the ordering process, we calculate phase transition rates following a phenomenological approach (34–36) to reproduce the observations of our neutron study. We define an order parameter Q as $1 - 2 \times \text{occ}(\text{D2})$ [or $2 \times \text{occ}(\text{D1}) - 1$] which quantifies the degree of ordering, i.e., $Q = 1$ for completely ordered ice VIII, $Q = 0$ for completely disordered ice VII, and $0 < Q < 1$ for partially disordered ice VIII (or partially ordered ice VII). Because the phase transition from ice VII to ice VIII is weakly first order accompanied by nucleation and growth, we apply well-known models of transition kinetics (35, 36): The rate of the phase transition from ice VII to ice VIII is set to be proportional to the difference of Gibbs free energy ΔG of the two phases, an Arrhenius term with an activation energy E_a , and the n th power of concentration of the reactant phase $(1 - Q)$. Thus, the kinetic rate law is expressed as (e.g., ref. 36)

$$\frac{dQ}{dt} = A \cdot \left(1 - \exp\left(\frac{\Delta G}{RT}\right)\right) \cdot \exp\left(-\frac{E_a}{RT}\right) \cdot (1 - Q)^n, \quad [1]$$

where A is a constant, t is time, R is the gas constant, and T is temperature. The excess Gibbs free energy at equilibrium temperature $[\Delta G(T_c)]$ can be written using the enthalpy difference (ΔH) and entropy difference (ΔS) between ice VII and ice VIII as following:

$$\Delta G(T_c) = \Delta H - T_c \Delta S = 0. \quad [2]$$

Thus, $\Delta H = T_c \Delta S$, and the temperature dependence of Gibbs free energy will be a linear function of temperature, given that ΔH and ΔS are temperature- and pressure independent:

$$\Delta G(T) = \Delta H - T \Delta S = T_c \Delta S - T \Delta S = (T_c - T) \Delta S. \quad [3]$$

Here we assume that ΔS is approximated by the Pauling entropy ($3.37 \text{ J mol}^{-1} \text{ K}^{-1}$). Furthermore, Eq. 1 can be written in the same manner for both rotation and translation with only a difference in the Arrhenius term which we assume to be a linear function of pressure, i.e., activation energies at zero pressure (E_{rot}^0 and E_{trs}^0) and activation volumes (γ_{rot} and γ_{trs}) for rotation and translation motions are

$$E_{rot} = E_{rot}^0 + \gamma_{rot} P \text{ and } E_{trs} = E_{trs}^0 + \gamma_{trs} P, \quad [4]$$

where P is pressure and E_{rot}^0 (E_{trs}^0) and γ_{rot} (γ_{trs}) are activation energies and activation volumes at zero pressure for rotation

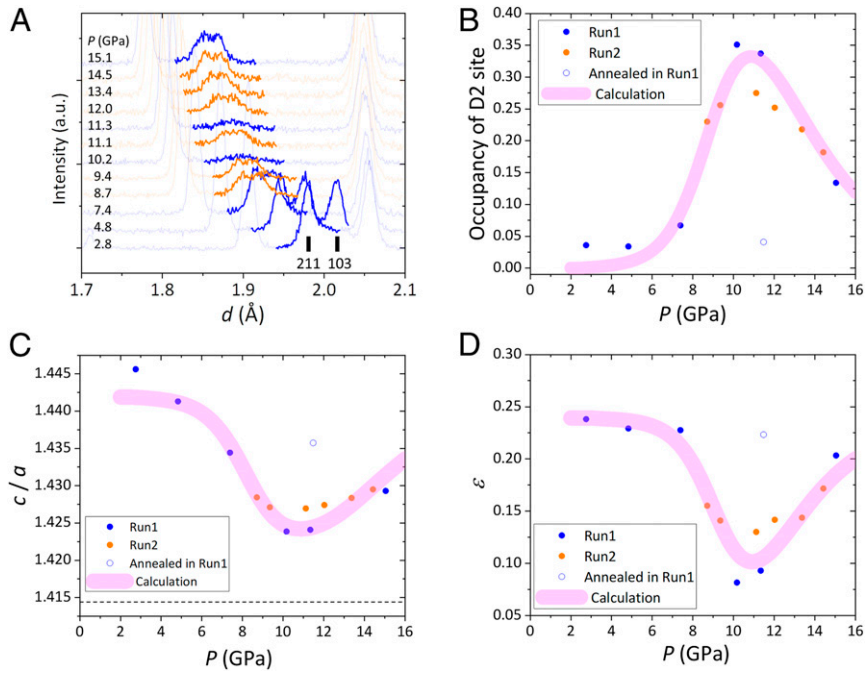


Fig. 2. (A) Neutron-diffraction patterns collected at 93 K, after rapid cooling (~ 6 K/min) of ice VII from 300 K at various pressures between 2.8 and 15.1 GPa. Specific 211 and 103 Bragg reflections of ice VIII are highlighted. Blue and orange profiles show the patterns taken in Run1 and Run2, respectively. Pressure dependences of (B) occupancy of D2 site, (C) the c/a axial ratio, and (D) the displacement of oxygen atom from ideal position in the cubic structure $\varepsilon (= 2c [1/8 - z(\text{O})])$, obtained from the Rietveld analysis. Blue and orange filled circles in B–D correspond to the data taken in Run1 and Run2, respectively, and blue open circles show the values for the annealed sample in Run1. A dashed line in C shows $\sqrt{2}$, which is the value of the ideal cubic ice VII. Pink broad lines in B–D show the results of the calculations based on the model discussed in the text for $n = 2$ in Eq. 5. The error bars are not shown as they are smaller than the symbols.

(translation). In our study the sample is cooled at a constant rate and the temperature T_i at any given time t_i is known. The time evolution of Q_{i+1} at a time t_{i+1} can then be obtained from Eqs. 1–4 as

$$\Delta Q = Q_{i+1} - Q_i = A \cdot \left(1 - \exp\left(\frac{\Delta S(T_c - T_i)}{RT_i}\right) \right) \cdot \left\{ \exp\left(\frac{E_{rot}^0 + \gamma_{rot}P}{RT_i}\right) + \exp\left(\frac{E_{trs}^0 + \gamma_{trs}P}{RT_i}\right) \right\} \cdot (1 - Q)^n \cdot \Delta t. \quad [5]$$

The numerical integration with sufficiently small time step gives Q at 93 K after rapid cooling. In the least-square fitting procedure, however, the parameters A, E_{rot}^0, E_{trs}^0 , are severely correlated and could not be simultaneously determined from Q at 93 K only.

In order to constrain the three parameters, additional neutron-diffraction measurements were carried out at 12.0 GPa on decreasing temperature from 300 K with 1.5 K/min cooling rate. Time-sliced diffraction data with 10-min intervals were refined from which the temperature variation of Q (Fig. 4B) was obtained by least-square fitting to minimize the difference between the observed and the calculated Q . The best fit was obtained with $n = 2$ (Fig. 4), yielding, $A = 3.0 \times 10^{12} \text{ s}^{-1}$, $E_{rot}^0 = 4.8 \times 10^4 \text{ J mol}^{-1}$, $\gamma_{rot} = 2.0 \times 10^3 \text{ J mol}^{-1} \cdot \text{GPa}^{-1}$, $E_{trs}^0 = 8.1 \times 10^4 \text{ J mol}^{-1}$, and $\gamma_{trs} = -1.2 \times 10^3 \text{ J mol}^{-1} \cdot \text{GPa}^{-1}$. Fitting with $n = 3$ differs hardly from $n = 2$, but fitting with $n = 1$ deviates clearly from the observed data, particularly for the temperature variation (Fig. 4). Regardless which n is chosen, the fitted parameters converge to approximately the same values within error, except for A . Despite the fitted parameters having errors of several

Table 1. Results of the Rietveld structure analyses for partially disordered ice VIII with the corresponding P - T conditions

Run	Data no.	P , GPa	T , K	a , Å	c , Å	c/a	V , Å ³	z (O)	y (D1)	z (D1)	occ(D2)	ε
Run1	30608	2.75(2)	93	4.6356(2)	6.7012(4)	1.44562(9)	143.998(9)	0.1072(4)	0.4179(4)	0.1947(2)	0.036(3)	0.2381(10)
	30625	4.83(4)	93	4.5559(2)	6.5665(4)	1.44131(12)	136.299(11)	0.1075(5)	0.4197(6)	0.1996(2)	0.034(4)	0.2292(13)
	30636	7.39(5)	93	4.4864(2)	6.4354(4)	1.43443(12)	129.527(10)	0.1073(4)	0.4219(6)	0.2027(2)	0.067(4)	0.2276(12)
	30647	10.17(6)	93	4.4300(3)	6.3077(9)	1.4239(2)	123.790(8)	0.1185(8)	0.4220(7)	0.2094(4)	0.351(5)	0.082(2)
	30657	11.34(6)	93	4.4041(3)	6.2719(8)	1.4241(2)	121.651(8)	0.1176(8)	0.4226(7)	0.2093(4)	0.337(5)	0.093(2)
	30659	11.48(7)	93*	4.3901(2)	6.3030(4)	1.43574(11)	121.474(9)	0.1073(4)	0.4269(6)	0.2060(2)	0.041(4)	0.2233(12)
	30675	15.05(10)	93	4.3312(2)	6.1906(3)	1.42930(9)	116.133(6)	0.1086(5)	0.4245(5)	0.2126(2)	0.134(4)	0.2034(11)
Run2	36353	8.71(3)	93	4.4565(2)	6.3658(5)	1.42844(12)	126.427(8)	0.1128(5)	0.4149(5)	0.2061(2)	0.230(3)	0.1552(13)
	36360	9.35(3)	93	4.4459(2)	6.3448(5)	1.42711(12)	125.414(6)	0.1139(5)	0.4157(5)	0.2062(2)	0.256(3)	0.1410(13)
	36376	11.12(4)	93	4.4083(2)	6.2904(7)	1.42696(17)	122.241(8)	0.1147(6)	0.4190(6)	0.2072(3)	0.275(4)	0.1301(18)
	36383	12.03(4)	93	4.3847(2)	6.2588(6)	1.42741(16)	120.329(8)	0.1137(5)	0.4165(6)	0.2105(3)	0.252(4)	0.142(2)
	36396	13.37(4)	93	4.3631(2)	6.2321(6)	1.42835(15)	118.641(8)	0.1135(5)	0.4200(6)	0.2087(3)	0.218(4)	0.144(2)
	36409	14.42(9)	93	4.3414(2)	6.2061(5)	1.42951(13)	116.970(8)	0.1112(5)	0.4201(6)	0.2099(2)	0.182(4)	0.1717(14)

*Cooled after annealing at 260 K for 2 h.

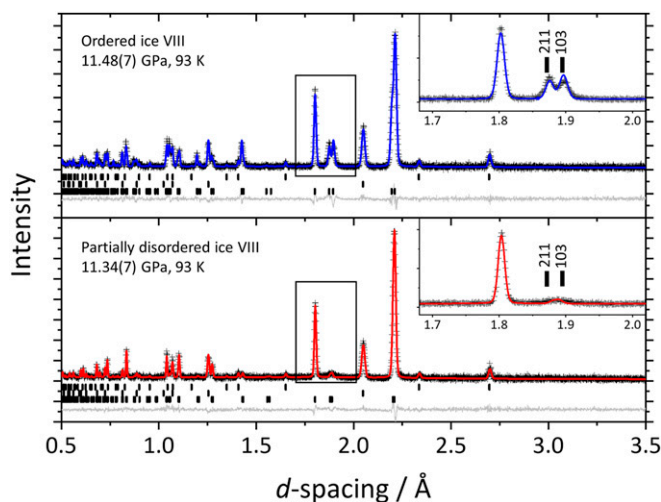


Fig. 3. Diffraction patterns with results of Rietveld refinements (line through the data). (Lower) Partially disordered ice VIII (no. 30657 in Run1) collected at 11.34(7) GPa and 93 K after the rapid cooling from 300 K. (Upper) Fully ordered ice VIII (no. 30659 in Run1) collected at 11.48(7) GPa and 93 K after cooling followed by annealing at 260 K for 2 h. (Insets) Enlarged patterns with the characteristic doublet peak of ice VIII. Tick marks at the bottom show the expected positions of Bragg reflections for ice VIII, diamond (anvil material), and lead (pressure marker), from bottom to top.

dozens of percent and considering the observed scattering of the occupancies and correlations among the parameters, the activation energy obtained here is still close to those obtained from dielectric measurements by Whalley et al. (37) at 2.3 GPa, i.e., $E^0 = 4.86 \times 10^4 \text{ J mol}^{-1}$ and $\gamma = 2.5(5) \times 10^3 \text{ J mol}^{-1} \cdot \text{GPa}^{-1}$. They are also close to the activation energies and activation volumes reported by Iitaka (32) for the DL (two hydrogens [D] or no hydrogen [L]) rotational defects and ionic (OH^- and H_3O^+ , denoted as \pm) defects calculated from electrical conductivity, $E_{DL}^0 = 4.85 \times 10^4 \text{ J mol}^{-1}$, $\gamma_{DL} = 2.5 \times 10^3 \text{ J mol}^{-1} \cdot \text{GPa}^{-1}$, $E_{\pm}^0 = 5.8 \times 10^4 \text{ J mol}^{-1}$, and $\gamma_{\pm} = -3.5 \times 10^3 \text{ J mol}^{-1} \cdot \text{GPa}^{-1}$. Note that the activation energy reported by Whalley et al. may correspond to rotational motion, although it is not explicitly described in the paper (37), because the rotational motion is expected to be dominant at 2.3 GPa. Also, the activation energies with respect to DL and ionic (\pm) defects reported in Iitaka correspond to the rotational and translational motions, respectively. Although the reported activation volumes differ by one order of magnitude (22, 33, 37, 38), which is probably because they were obtained by very different technique and different analytical methods,

a negative value of γ_{tr} is commonly observed in measurements of electrical conductivity (22, 32), X-ray induced dissociation (33), and the overtone mode in Raman spectra (38). The coefficients in the activation energies described in Eq. 4 may be further divided into several terms with respect to the formation and mobility of four types of defects (D, L, +, -). The observed negative γ_{tr} should be due to the activation volumes of its formation and/or mobility. In the case of ice I_h , the activation volumes of formation of all of the four types of defects show positive values, derived from measurements of high-frequency conductivity and pseudopiezoelectric effect (20). A better understanding of the motion of defects in ice VII would be highly desirable. Once the order parameter Q is obtained as a function of pressure, the c/a ratio and ϵ can be expressed as a polynomial up to second order in Q (36) following Landau theory:

$$\frac{c}{a} = \sqrt{2} + s_1 Q + s_2 Q^2,$$

$$\epsilon = s'_1 Q + s'_2 Q^2, \quad [6]$$

where s_1 and s_2 and their primes are coefficients adjusted to the observed data, yielding $2.5(4) \times 10^{-2}$ and $2(5) \times 10^{-3}$ for c/a , and $3.5(3) \times 10^{-1}$ and $-1.1(3) \times 10^{-1}$ for ϵ , respectively. With these values the pressure dependence of c/a and ϵ are shown in Fig. 2 C and D.

The fact that there is a remarkably good agreement between the model and the observed data (Figs. 2 and 4) on simultaneously the hydrogen occupancy, the c/a ratio, and the tetragonal distortion ϵ strongly indicates that it correctly describes the essential physics of the hydrogen order-disorder transition in ice VII-VIII.

The discovery of extremely slow transition kinetics and the resulting possibility of partially disordered ice VIII may explain reports of various anomalies observed experimentally at ~ 10 GPa. To give two examples, the Raman peak width of the symmetric vibration mode of ice VII was reported to have a minimum at around 11–13 GPa (39) which was attributed (40) to potential H-ordering. The origin of this minimum could indeed be a change in hydrogen motions since peak width in Raman spectra is generally proportional to the inverse of the relaxation time. A minimum would hence arise when the relaxation times become very long. Another example is the reported splitting of Bragg reflections observed in X-ray diffraction on ice VII at 11–14 GPa, both in hydrogenated (41) and deuterated samples (42, 43), indicating that ice VII is no longer cubic. The splitting of the 110 peak (in cubic indexing) may be attributed to a short-range ordering as a result of fluctuation which freeze in due to the proximity of the phase

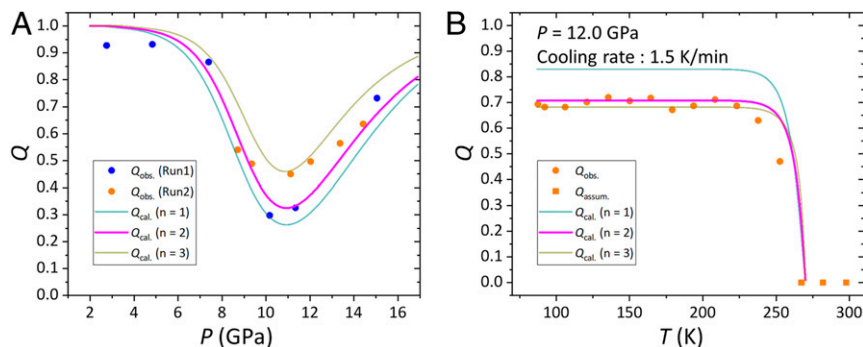


Fig. 4. Comparison of fitting results of the calculations based on phenomenological models with $n = 1-3$ in Eq. 5 in terms of (A) the order parameters (Q) obtained from the measured occupancies of D2 site at 93 K at elevated pressures, and (B) the increase of Q with decreasing temperature at 12.0 GPa with a cooling rate of 1.5 K/min. Q values above the phase transition temperatures are assumed to be 0, shown as squares in B.

boundary to ice VIII. From our observation and from previous studies in other high-pressure ices (26, 44–47), the axial ratio is very sensitive to the change of H-ordering. In the most disordered ice VIII of our study, for example (no. 30657 in Run1, Fig. 3), the doublet at 1.9 Å was barely visible but the refined order parameter was still 0.38. This fact implies that the c/a ratio is more sensitive at weak H-ordering in ice VII than the intensity of the doublet, i.e., that neutron experiments—including this study—could not easily detect evidence of small partial ordering of ice VII. In general, substantial ordering may still exist over short-range distances and for short time as fluctuation even above the phase transition temperature (34). If such fluctuation freezes due to the slow motion of hydrogens, the ordered domain may persist enough to detect.

We finally want to point out an interesting connection with H-ordering phenomena in other high-pressure polymorphs, such as the recently studied ordering in ice VI–XV [see details in a review paper by Salzmann (48) and its references]. These occur in the 80–130 K range with the aid of dissolved dopants such as HCl. It appears that the timescale for H-ordering and applied cooling rates are very similar to the one in our experiments at 10 GPa and ~150 K higher temperatures. We therefore expect similar phenomena to exist in the case of the ice VII–VIII transition, such as the existence of “deep glassy states” (27, 29) at sufficiently high cooling rates and the presence of a low-temperature endotherm as well as transient-hydrogen ordering upon heating. The remarkable difference is that in ice VII–VIII it would be observable in pure ice and at temperatures close to ambient, although at considerably higher pressures.

Methods

Neutron Diffraction. Neutron-diffraction experiments were conducted at the beamline PLANET (49) at the Material and Life Science Experimental Facility of J-PARC, Ibaraki, Japan. Deuterated water (99.6% D) from Eurisotop with small pieces of highly pure lead from New Metals and Chemicals Ltd. as a pressure calibrant were loaded into encapsulating TiZr null scattering metal gaskets. The gaskets were sandwiched by a pair of sintered diamond double-

toroidal anvils, and loaded into a “Mito system” load frame (46). This system allows a precise control of temperature as well as rapid heating/cooling by controlling the flow rate of liquid nitrogen coolant. Two separate runs with identical cell setups were performed. The sample pressure was determined from the observed lattice parameter of lead using the known equation of state (EOS) of lead (below 14 GPa) (50), or using the EOS of ice VIII above 14 GPa (51). The sample position was aligned by scanning to maximize the sample scattering intensity. The Rietveld analyses were performed using the GSAS (52) with EXPGUI (53) packages on the diffraction patterns containing mixed phases of sample, diamond (anvils), and lead.

Ice VIII has tetragonal crystal system with space group $I4_1/amd$, and the oxygen atoms at $[0, 1/4, z(O)]$ and the deuterium atoms at $[0, y(D1), z(D1)]$. In addition to the original deuterium site (D1), the D2 site is also considered for the partial disorder model as described in the main text. More detailed procedures for sample setup, P - T control, data reduction, and refinements were described elsewhere (54).

The sample at ~0.1 GPa was first cooled to 240 K and compressed to 3.3 GPa at 240 K in order to produce a fine powder of ice VIII through several solid–solid phase transitions (Fig. 1). Then, the sample was annealed at 300 K to release deviatoric stresses, followed by compression to the target pressure. At each pressure point, the sample was then rapidly cooled (~6 K/min) to 93 K, and neutron-diffraction patterns were collected at this temperature. Further compression was carried out after warming up to 300 K. This cycle was repeated up to 15.1 GPa in Run1 and 14.4 GPa in Run2, respectively. Experimental P - T conditions and the results of structure analyses are shown in Table 1. At 11.4 GPa in Run1, a diffraction pattern was taken on a sample which was annealed for 2 h at 260 K in order to make well-ordered ice VIII. At 12.0 GPa in Run2, diffraction data were collected at continuously decreasing temperature from 300 to 93 K at a cooling rate of 1.5 K.

Data Availability. All data are included in the manuscript and available from the corresponding author upon request.

ACKNOWLEDGMENTS. We are grateful to Dr. J. Abe and Dr. K. Funakoshi for their assistance with the experiments. Neutron-diffraction experiments were performed through the J-PARC user programs (2016I0011 and 2017I0011). This study was supported by Japan Society for the Promotion of Science (JSPS) KAKENHI (Grants 18H05224, 18H01936, and 15H05829) and JSPS-CNRS bilateral joint research project PRC 2191.

- W. F. Kuhs, J. L. Finney, C. Vettier, D. V. Bliss, Structure and hydrogen ordering in ices VI, VII, and VIII by neutron powder diffraction. *J. Chem. Phys.* **81**, 3612–3623 (1984).
- Y. Takii, K. Koga, H. Tanaka, A plastic phase of water from computer simulation. *J. Chem. Phys.* **128**, 204501 (2008).
- J. L. Aragones, M. M. Conde, E. G. Noya, C. Vega, The phase diagram of water at high pressures as obtained by computer simulations of the TIP4P/2005 model: The appearance of a plastic crystal phase. *Phys. Chem. Chem. Phys.* **11**, 543–555 (2009).
- J. L. Aragones, C. Vega, Plastic crystal phases of simple water models. *J. Chem. Phys.* **130**, 244504 (2009).
- K. Himoto, M. Matsumoto, H. Tanaka, Lattice- and network-structure in plastic ice. *Phys. Chem. Chem. Phys.* **13**, 19876–19881 (2011).
- C. Cavazzoni *et al.*, Superionic and metallic states of water and ammonia at giant planet conditions. *Science* **283**, 44–46 (1999).
- N. Goldman, L. E. Fried, I. F. W. Kuo, C. J. Mundy, Bonding in the superionic phase of water. *Phys. Rev. Lett.* **94**, 217801 (2005).
- T. R. Mattsson, M. P. Desjarlais, Phase diagram and electrical conductivity of high energy-density water from density functional theory. *Phys. Rev. Lett.* **97**, 017801 (2006).
- H. F. Wilson, M. L. Wong, B. Militzer, Superionic to superionic phase change in water: Consequences for the interiors of Uranus and Neptune. *Phys. Rev. Lett.* **110**, 151102 (2013).
- J. Sun, B. K. Clark, S. Torquato, R. Car, The phase diagram of high-pressure superionic ice. *Nat. Commun.* **6**, 8156 (2015).
- J.-A. Hernandez, R. Caracas, Superionic-superionic phase transitions in body-centered cubic H₂O ice. *Phys. Rev. Lett.* **117**, 135503 (2016).
- J. A. Hernandez, R. Caracas, Proton dynamics and the phase diagram of dense water ice. *J. Chem. Phys.* **148**, 214501 (2018).
- E. Sugimura *et al.*, Experimental evidence of superionic conduction in H₂O ice. *J. Chem. Phys.* **137**, 194505 (2012).
- M. Millot *et al.*, Experimental evidence for superionic water ice using shock compression. *Nat. Phys.* **14**, 297–302 (2018).
- M. Millot *et al.*, Nanosecond X-ray diffraction of shock-compressed superionic water ice. *Nature* **569**, 251–255 (2019).
- S. Klotz *et al.*, Metastable ice VII at low temperature and ambient pressure. *Nature* **398**, 681–684 (1999).
- S. Klotz, L. E. Bove, T. Strässle, T. C. Hansen, A. M. Saitta, The preparation and structure of salty ice VII under pressure. *Nat. Mater.* **8**, 405–409 (2009).
- S. Klotz *et al.*, Ice VII from aqueous salt solutions: From a glass to a crystal with broken H-bonds. *Sci. Rep.* **6**, 32040 (2016).
- C. G. Salzmann *et al.*, Ammonium fluoride as a hydrogen-disordering agent for ice. *J. Phys. Chem. C* **123**, 16486–16492 (2019).
- V. F. Petrenko, R. W. Whitworth, *Physics of Ice* (Oxford University Press, Oxford, 1999).
- H. Zheng *et al.*, The electrical conductivity of H₂O at 0.21–4.18 GPa and 20–350°C. *Chin. Sci. Bull.* **42**, 969–976 (1997).
- T. Okada, T. Iitaka, T. Yagi, K. Aoki, Electrical conductivity of ice VII. *Sci. Rep.* **4**, 5778 (2014).
- E. Katoh, H. Yamawaki, H. Fujihisa, M. Sakashita, K. Aoki, Protonic diffusion in high-pressure ice VII. *Science* **295**, 1264–1266 (2002).
- N. Noguchi, T. Okuchi, Self-diffusion of protons in H₂O ice VII at high pressures: Anomaly around 10 GPa. *J. Chem. Phys.* **144**, 234503 (2016).
- A. N. Dunaeva, D. V. Antsyshkin, O. L. Kuskov, Phase diagram of H₂O: Thermodynamic functions of the phase transitions of high-pressure ices. *Sol. Syst. Res.* **44**, 202–222 (2010).
- T. M. Gasser *et al.*, Experiments indicating a second hydrogen ordered phase of ice VI. *Chem. Sci.* **9**, 4224–4234 (2018).
- A. Rosu-Finsen, C. G. Salzmann, Origin of the low-temperature endotherm of acid-doped ice VI: New hydrogen-ordered phase of ice or deep glassy states? *Chem. Sci.* **10**, 515–523 (2018).
- A. V. Thoeny, T. M. Gasser, T. Loerting, Distinguishing ice β-XV from deep glassy ice VI: Raman spectroscopy. *Phys. Chem. Chem. Phys.* **21**, 15452–15462 (2019).
- A. Rosu-Finsen, A. Amon, J. Armstrong, F. Fernandez-Alonso, C. G. Salzmann, Deep-glassy ice VI revealed with a combination of neutron spectroscopy and diffraction. *J. Phys. Chem. Lett.* **11**, 1106–1111 (2020).
- C. Jaccard, Theoretical and experimental studies of the electrical properties of ice. *Helv. Phys. Acta* **32**, 89–128 (1959).
- C. Jaccard, Thermodynamics of irreversible processes applied to ice. *Phys. Kondens. Mater.* **3**, 99–118 (1964).
- T. Iitaka, Simulating proton dynamics in high-pressure ice. *Rev. High Pressure Sci. Technol.* **23**, 124–132 (2013).
- H. Fukui, N. Hiraoka, N. Hirao, K. Aoki, Y. Akahama, Suppression of X-ray-induced dissociation of H₂O molecules in dense ice under pressure. *Sci. Rep.* **6**, 26641 (2016).
- L. D. Landau, E. M. Lifshitz, *Course on Theoretical Physics* (Pergamon Press, 1976).
- E. Salje, Kinetic rate laws as derived from order parameter theory I: Theoretical concepts. *Phys. Chem. Miner.* **15**, 336–348 (1988).

36. A. Putnis, *An Introduction to Mineral Sciences* (Cambridge University Press, 1992).
37. E. Whalley, D. W. Davidson, J. B. R. Heath, Dielectric properties of ice VII. Ice VIII: A new phase of ice. *J. Chem. Phys.* **45**, 3976–3982 (1966).
38. C. F. Larsen, Q. Williams, Overtone spectra and hydrogen potential of H₂O at high pressure. *Phys. Rev. B* **58**, 8306–8312 (1998).
39. P. Pruzan, J. C. Chervin, M. Gauthier, Raman spectroscopy investigation of ice VII and deuterated ice VII to 40 GPa. Disorder in ice VII. *Europhys. Lett.* **13**, 81–87 (1990).
40. P. Loubeyre, R. LeToullec, E. Wolarin, M. Hanfland, D. Husermann, Modulated phases and proton centring in ice observed by x-ray diffraction up to 170 GPa. *Nature* **397**, 503–506 (1999).
41. M. Somayazulu *et al.*, In situ high-pressure x-ray diffraction study of H₂O ice VII. *J. Chem. Phys.* **128**, 064510 (2008).
42. H. Hirai, H. Kadobayashi, T. Matsuoka, Y. Ohishi, Y. Yamamoto, High pressure x-ray diffraction and Raman spectroscopic studies of the phase change of D₂O ice VII at approximately 11 GPa. *High Pressure Res.* **34**, 289–296 (2014).
43. H. Kadobayashi, H. Hirai, T. Matsuoka, Y. Ohishi, Y. Yamamoto, A possible existence of phase change of deuterated ice VII at about 11 GPa by X-ray and Raman studies. *J. Phys. Conf. Ser.* **500**, 182017 (2014).
44. C. G. Salzmann, A. Hallbrucker, J. L. Finney, E. Mayer, Raman spectroscopic features of hydrogen-ordering in ice XII. *Chem. Phys. Lett.* **429**, 469–473 (2006).
45. C. G. Salzmann, P. G. Radaelli, E. Mayer, J. L. Finney, Ice XV: A new thermodynamically stable phase of ice. *Phys. Rev. Lett.* **103**, 105701 (2009).
46. K. Komatsu *et al.*, Development of a new P–T controlling system for neutron-scattering experiments. *High Press. Res.* **33**, 208–213 (2013).
47. C. G. Salzmann *et al.*, Detailed crystallographic analysis of the ice VI to ice XV hydrogen ordering phase transition. *J. Chem. Phys.* **145**, 204501 (2016).
48. C. G. Salzmann, Advances in the experimental exploration of water's phase diagram. *J. Chem. Phys.* **150**, 060901 (2019).
49. T. Hattori *et al.*, Design and performance of high-pressure PLANET beamline at pulsed neutron source at J-PARC. *Nucl. Instrum. Methods Phys. Res. Sect. A* **780**, 55–67 (2015).
50. T. Strässle, S. Klotz, K. Kunc, V. Pomjakushin, J. S. White, Equation of state of lead from high-pressure neutron diffraction up to 8.9 GPa and its implication for the NaCl pressure scale. *Phys. Rev. B Condens. Matter Mater. Phys.* **90**, 014101 (2014).
51. S. Klotz *et al.*, Bulk moduli and equations of state of ice VII and ice VIII. *Phys. Rev. B* **95**, 174111 (2017).
52. A. Larson, R. Von Dreele, "General structure analysis system (GSAS)" (Tech. Rep. LAUR-86-748, Los Alamos National Laboratory, 2004).
53. B. Toby, EXPGUI, a graphical user interface for GSAS. *J. Appl. Crystallogr.* **34**, 210–213 (2001).
54. K. Komatsu *et al.*, Crystal structure of magnesium dichloride decahydrate determined by X-ray and neutron diffraction under high pressure. *Acta Crystallogr. B Struct. Sci. Cryst. Eng. Mater.* **71**, 74–80 (2015).